MEAM 5360: Fluid Mechanics Term Project

Numerical Investigation of Flow Past a Circular Cylinder

Joshua Dalal and Jason de Gentile

Executive Summary

This report presents a CFD study of two-dimensional, incompressible flow past a circular cylinder confined within a channel using ANSYS Fluent. Simulations were performed at Reynolds numbers of Re = 0.1, 1, 10, 100, and 1000 to investigate drag behavior, wake development, and the onset of flow instabilities. A mesh independence study showed that an 11,259-element mesh with boundary-layer inflation produced results nearly identical to finer meshes while significantly reducing computational cost. At low Reynolds numbers, the flow remained nearly symmetric and viscosity-dominated, while increasing Re produced wake separation, recirculation, and eventually periodic vortex shedding. Transient simulations showed no sustained oscillations at Re = 10, while clear Kármán vortex shedding developed at Re = 100 and above. Overall, the results illustrate the transition from creeping flow to inertia-dominated unsteady flow as Reynolds number increases.

1. Introduction

In this study, ANSYS Fluent was used to simulate two-dimensional incompressible flow past a circular cylinder inside a channel. Flow past a bluff body is a classic problem in fluid mechanics that we have covered in a number of different classes. At very low Reynolds numbers, viscous forces dominate and the flow remains nearly symmetric around the cylinder. As Reynolds number increases, inertial effects become more important, leading to wake formation, flow separation, and eventually periodic vortex shedding in the form of a Kármán vortex street.

2. Methods

2.1 Geometry and Boundary Conditions

The computational domain consisted of a two-dimensional rectangular channel with a height of H = 8 m containing a circular cylinder of diameter d = 1 m centered vertically within the channel. The inlet was positioned 10 cylinder diameters upstream of the cylinder center, while the outlet extended 30 diameters downstream to allow the wake to develop without significant outlet effects. A uniform inlet velocity was prescribed at the inlet boundary. The inlet was positioned 10 cylinder diameters upstream of the cylinder center to minimize inlet effects and allow the flow to develop before interacting with the cylinder. No-slip boundary conditions were imposed on the channel walls and cylinder surface. Fluid properties were set where $\rho = 1$ kg/m³ and $\mu = 1$ Pa·s, so that the Reynolds number was numerically equal to the inlet velocity.

2.2 Mesh and Independence Study

Five progressively refined hybrid meshes were generated in ANSYS Meshing, ranging from 4,769 to 39,163 elements. Boundary-layer inflation was added around the cylinder surface in the finer meshes to better capture near-wall velocity gradients and wake behavior. A mesh independence study was performed at Re = 10 by comparing the computed drag force for each mesh. Results showed negligible change between the 11,259-element mesh and the finest mesh tested, indicating that the solution was effectively mesh independent. The 11,259-element mesh was therefore selected for the remainder of the simulations as a compromise between accuracy and computational cost.

Table 1. Mesh Independence Study (Re = 10)

Mesh Size (elements)	Features	F^d (N/m)
4,769	No inflation	320.392
5,927	Inflation around cylinder	260.532
11,259	Inflation + downstream face sizing	258.313
22,046	Same as mesh 3, finer	258.309
39,163	Same as mesh 4, finer	258.307

2.3 Solver Settings

ANSYS Fluent 2025 was used to solve the incompressible Navier–Stokes equations using a pressure-based solver with the SIMPLE pressure–velocity coupling scheme. Second-order spatial discretization was applied to improve numerical accuracy. Steady-state simulations were first performed for Re = 0.1, 1, 10, and 100 until all residuals reached convergence. Transient simulations were then carried out at Re = 10, 100, and 1000 using a second-order implicit time-stepping scheme to capture unsteady wake behavior and vortex shedding. During each case, drag and lift forces acting on the cylinder were monitored to evaluate convergence and identify the onset of flow oscillations.

2.4 Post-Processing and Correlations

Velocity magnitude contours, static pressure contours, streamline plots, vorticity contours, and streamwise velocity profiles were extracted to analyze the flow structure at each Reynolds number. MATLAB was used to calculate the drag coefficient using the simulated drag force values and to compare the CFD results with analytical and empirical drag correlations, including the Lamb creeping-flow solution, the Sucker–Brauer correlation, and the White correlation. Experimental data from Tritton were also included for comparison with the numerical results.

3. Results and Discussion

3.1 Drag Force and Drag Coefficient

Table 2 summarizes the computed drag force and drag coefficient for each Reynolds number tested. As Reynolds number increased, the drag coefficient decreased while the total drag force increased due to the increasing flow velocity and dynamic pressure. The CFD results followed the same general trend as the empirical drag correlations, although the simulated drag coefficients were consistently higher at lower Reynolds numbers. We believe this difference is primarily attributed to the confined two-dimensional channel geometry used in the simulations, which increases blockage effects compared to the unconfined flows assumed in the analytical and empirical correlations. At higher Reynolds numbers, the CFD results showed closer agreement with the published correlations as inertial effects became more dominant.

Table 2. Summary of CFD Results

Re	U (m/s)	F_d (N/m)	C_d (CFD)	C^d (Sucker–Brauer)
0.1	0.1	1.5496	309.92	53.96
1	1	16.030	32.06	7.98
10	10	258.31	5.166	2.056
100	100	7858.7	1.572	1.293
1000	1000	626,773	1.254	1.195

Figure 1 shows the variation of drag coefficient with Reynolds number on a log–log scale. The CFD results follow the same overall decreasing trend as the Sucker–Brauer and White correlations, although the simulated drag coefficients are consistently higher at low Reynolds numbers. At Re = 0.1, the CFD result gives (C_d = 309.92), compared to 53.96 from the Sucker–Brauer correlation. At Re = 1, the CFD value decreases to 32.06 while the Sucker–Brauer prediction is 7.98. As Reynolds number increases, the agreement improves: at Re = 10, the CFD result is (C_d = 5.166), compared to 2.056 from Sucker–Brauer and approximately 5.64 from the White correlation. By Re = 100 and 1000, the CFD results of 1.572 and 1.254 are much closer to the empirical predictions, indicating that the influence of confinement becomes less significant at higher Reynolds numbers.

Figure 2 shows the drag force as a function of Reynolds number. Although the drag coefficient decreases with increasing Reynolds number, the total drag force increases substantially because the flow velocity and dynamic pressure increase. The CFD drag force rises from 1.55 N/m at Re = 0.1 to 258.3 N/m at Re = 10, eventually reaching 7,859 N/m at Re = 100 and 626,773 N/m at Re = 1000. The CFD results follow the same general trend as the Sucker–Brauer correlation at moderate and high Reynolds numbers, while larger deviations occur at low Reynolds numbers due to the confined two-dimensional geometry and stronger viscous effects.

3.2 Steady-State Flow Field Evolution

Figures 3–5 show the steady-state velocity and pressure fields for Re = 0.1, 1, and 10, along with the steady Re = 100 solution prior to transient analysis. At Re = 0.1 (Figure 3), the flow is nearly symmetric upstream and downstream of the cylinder, characteristic of creeping (Stokes) flow. The velocity contours show no flow separation or wake formation, and the pressure field varies smoothly around the cylinder. The velocity profiles remain smooth and symmetric, with no reverse flow present. Viscous effects dominate the entire domain, and the flow disturbance extends several diameters upstream and downstream of the cylinder.

At Re = 1 (Figure 4), slight fore–aft asymmetry begins to develop as inertial effects become more important. The downstream velocity deficit becomes more noticeable, although the flow remains fully attached and symmetric about the centerline. The pressure contours show a larger downstream pressure drop compared to Re = 0.1, indicating increasing pressure-drag contribution. Velocity profiles downstream of the cylinder show reduced centerline velocity and slower wake recovery.

At Re = 10 (Figure 5), a clearly defined separated wake forms behind the cylinder. The velocity contours show a long low-velocity region extending downstream, while the pressure contours reveal a pronounced low-pressure wake associated with increasing form drag. The velocity profiles at x=2 show a strong velocity deficit and near-zero centerline velocity, indicating the presence of a symmetric recirculation region behind the cylinder. Further downstream, the profiles gradually recover toward the inlet distribution. Despite the separated wake, the flow remains steady and symmetric at this Reynolds number.

A steady-state simulation was also performed at Re = 100 prior to transient analysis (Figure 6). The steady solution produces a long separated wake with a substantial downstream velocity deficit and a large low-pressure region behind the cylinder. The drag force converges to a constant value during the steady-state iterations, indicating numerical convergence of the steady solver. Physically, however, flow at this Reynolds number is known to be unstable, and the steady solution represents only the time-averaged symmetric state before vortex shedding develops in the transient simulations.

Across all steady-state cases, the primary trends are increasing wake length, stronger downstream velocity deficits, and increasing pressure asymmetry as Reynolds number increases. These results illustrate the transition from viscosity-dominated creeping flow at low Reynolds number to inertia-dominated separated flow at higher Reynolds number.

3.3 Transient Flow Behavior and Instability Onset

Transient simulations were performed at Re = 10, 100, and 1000 to investigate the onset and evolution of unsteady vortex shedding. At Re = 10 (Figure 7), the lift and drag force histories rapidly converge to nearly constant values after a short startup transient. No sustained oscillations are observed in either signal, confirming that the flow remains stable despite the presence of a symmetric recirculation region behind the cylinder. The velocity contours show a steady attached wake with symmetric standing vortices, consistent with stable separated flow below the critical Reynolds number for periodic shedding.

At Re = 100 (Figure 8), the flow becomes fully unsteady and periodic vortex shedding develops. The lift force history initially grows from small disturbances before reaching a sustained oscillatory limit cycle, indicating the onset of a hydrodynamic instability. Velocity and vorticity contours show alternating vortices being shed from opposite sides of the cylinder, forming a well-defined Kármán vortex street downstream. The centerline velocity distribution and streamwise velocity profiles show strong wake oscillations, reverse flow near the cylinder, and delayed downstream recovery compared to the steady Re = 10 case. These results demonstrate the transition from steady separated flow to periodic unsteady shedding.

At Re = 1000 (Figure 9), the transient behavior becomes significantly more energetic. Large-amplitude lift and drag oscillations are present throughout the simulation, and the wake contains a long sequence of alternating vortical structures extending many cylinder diameters downstream. The vorticity contours show a fully developed vortex street with persistent wake oscillations and strong downstream velocity deficits. Although the simulation remains two-dimensional, the results qualitatively illustrate the increasingly unsteady nature of high-Reynolds-number bluff-body flow.

Comparing the transient cases, periodic vortex shedding is absent at Re = 10 but clearly present at Re = 100 and 1000, indicating that the critical Reynolds number for instability in this channel configuration lies between these two values. Overall, the transient simulations capture the transition from stable separated flow to sustained unsteady wake dynamics as inertial effects become dominant. Additional transient-flow visualizations are provided in the attached videos linked at the bottom of page 15, including one video for the Re = 100 transient case and one for the Re = 1000 transient case.

4. Conclusions

This study used ANSYS Fluent to investigate two-dimensional incompressible flow past a circular cylinder in a confined channel over Reynolds numbers ranging from 0.1 to 1000. The following key findings were obtained:

1. A mesh independence study showed that the 11,259-element mesh produced results nearly identical to the finest mesh tested while maintaining significantly lower computational cost, confirming that the numerical solution was effectively mesh independent.
2. The computed drag coefficient decreased with increasing Reynolds number, while the total drag force increased due to the increasing dynamic pressure of the flow. CFD drag coefficients were consistently higher than the Sucker–Brauer and White correlations at low Reynolds numbers because of the confined two-dimensional channel geometry used in the simulations. Agreement with the empirical correlations improved substantially at higher Reynolds numbers.
3. The steady-state simulations captured the transition from viscosity-dominated creeping flow to inertia-dominated separated flow. At Re = 0.1 and 1, the flow remained attached and nearly symmetric. By Re = 10, a steady separated wake and recirculation region formed behind the cylinder, producing a significant downstream velocity deficit and increased pressure drag.
4. Transient simulations showed that periodic vortex shedding was absent at Re = 10 but clearly developed at Re = 100 and 1000. At Re = 100, alternating vortices formed a distinct Kármán vortex street accompanied by sustained lift oscillations, indicating the onset of hydrodynamic instability. These results place the critical Reynolds number for instability in this confined geometry between Re = 10 and 100.
5. The simulations successfully reproduced the major flow features associated with bluff-body flow over a wide Reynolds number range, including wake formation, flow separation, recirculation, and vortex shedding. Overall, the results provide a clear illustration of the transition from stable creeping flow to highly unsteady wake dynamics as inertial effects become dominant.

References

(1) Lamb, H. Hydrodynamics, 6th ed.; Cambridge University Press: Cambridge, UK, 1932.

(2) Williamson, C. H. K. Vortex Dynamics in the Cylinder Wake. Annu. Rev. Fluid Mech. 1996, 28, 477–539.

(3) Zdravkovich, M. M. Flow Around Circular Cylinders, Vol. 1: Fundamentals; Oxford University Press: Oxford, UK, 1997.

(4) Sucker, D.; Brauer, H. Fluiddynamik bei der angestromten Zylindern. Wärme- Stoffübertrag. 1975, 8, 149–158.

(5) White, F. M. Fluid Mechanics, 8th ed.; McGraw-Hill: New York, 2016.

(6) Tritton, D. J. Experiments on the Flow Past a Circular Cylinder at Low Reynolds Numbers. J. Fluid Mech. 1959, 6, 547–567.

Figures

Mesh

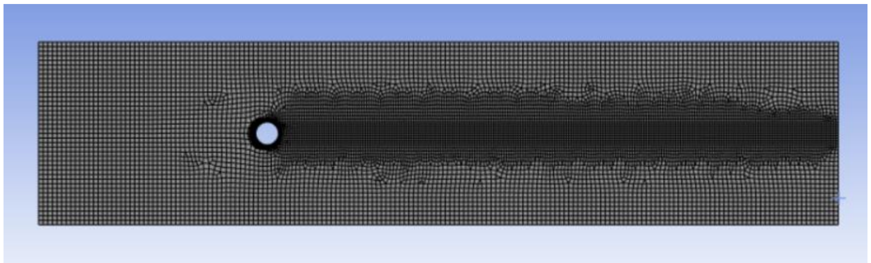

Figure M1. Overview of the computational mesh (11,259 elements) showing structured quadrilateral elements with boundary-layer inflation around the cylinder and refined face-sizing in the downstream wake region.

Check Mesh Quality	Yes, Errors
Target Skewness	Default (0.9)
Smoothing	Medium
Mesh Metric	Element Quality
Min	0.13542
Max	1.
Average	0.95326
Standard Deviation	0.11209

Check Mesh Quality	Yes, Errors
Target Skewness	Default (0.9)
Smoothing	Medium
Mesh Metric	Skewness
Min	1.3057e-010
Max	0.98916
Average	6.043e-002
Standard Deviation	0.10671

Figure M2. Mesh quality statistics: element quality (left; average 0.953) and skewness (right; average 6.04×10^{-2}), both indicating high mesh quality.

Figure 1. Drag Coefficient vs. Reynolds Number

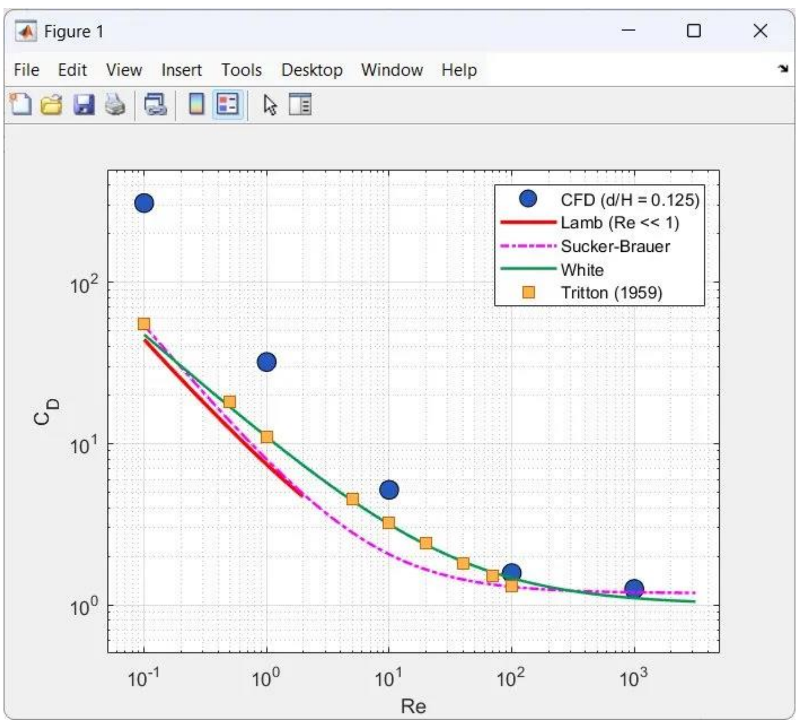

Figure 1. Log–log plot of drag coefficient C^d versus Reynolds number Re. Blue circles: CFD data (d/H = 0.125 confinement). Red solid line: Lamb's analytical solution for creeping flow (Re ≪ 1). Magenta dash-dot: Sucker–Brauer correlation. Green solid: White correlation. Orange squares: Tritton (1959) experimental data. The systematic upward shift of CFD data relative to the sphere-based correlations reflects the 2D channel confinement geometry.

Figure 2. Drag Force vs. Reynolds Number

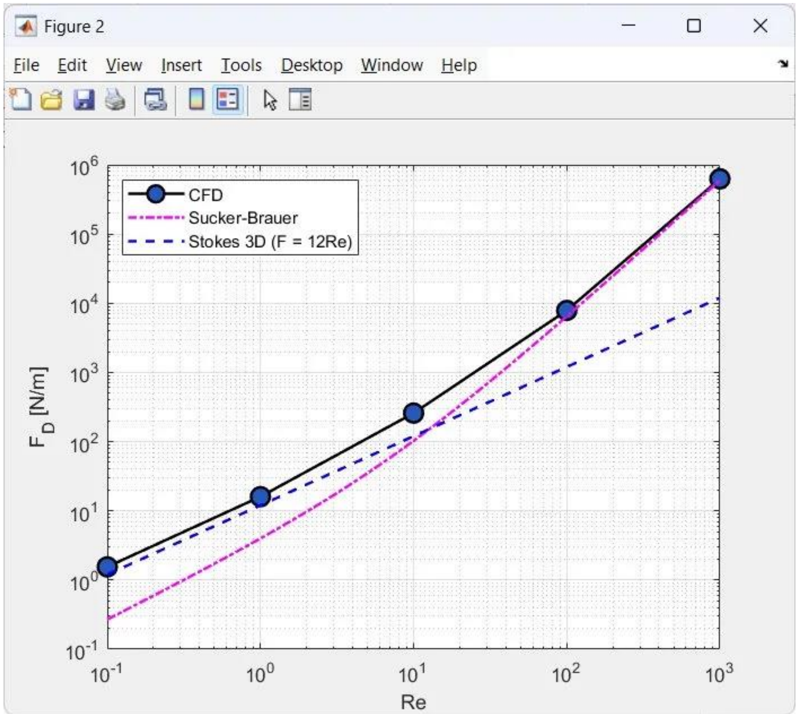

Figure 2. Log–log plot of drag force F^d (N/m) versus Re. Blue circles with connecting line: CFD data. Magenta dash-dot: Sucker–Brauer correlation. Blue dashed: Stokes 3D reference curve (F = 12Re, for a sphere). The CFD data track closely with Sucker–Brauer at Re ≥ 10 while the Stokes curve significantly under-predicts at high Re.

Figure 3. Flow Field at Re = 0.1 (Creeping Flow)

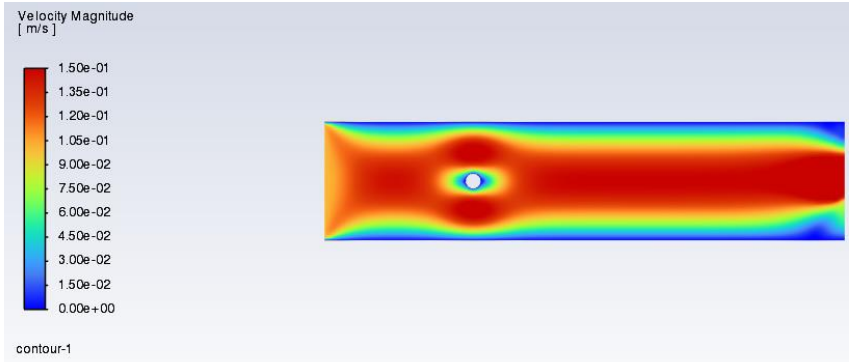

Figure 3a. Velocity magnitude contour at Re = 0.1 showing nearly symmetric creeping flow dominated by viscous effects, with no wake separation present.

Figure 3b. Static pressure contour at Re = 0.1 showing smooth pressure recovery and a broad upstream influence characteristic of Stokes flow.

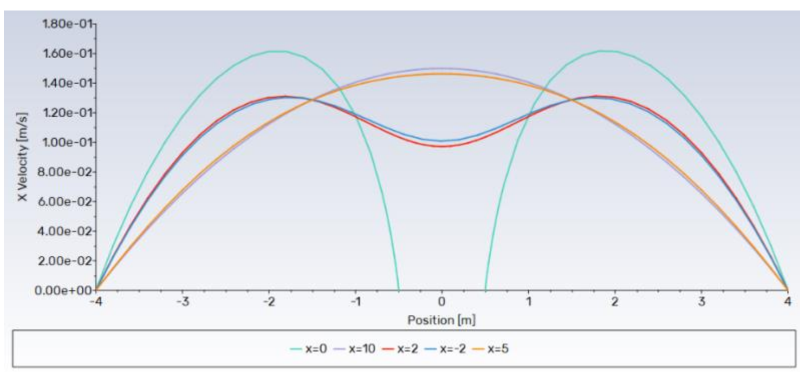

Figure 3c. Streamwise velocity profiles at Re = 0.1 showing smooth, symmetric behavior with no reverse flow or recirculation region.

Figure 4. Flow Field at Re = 1

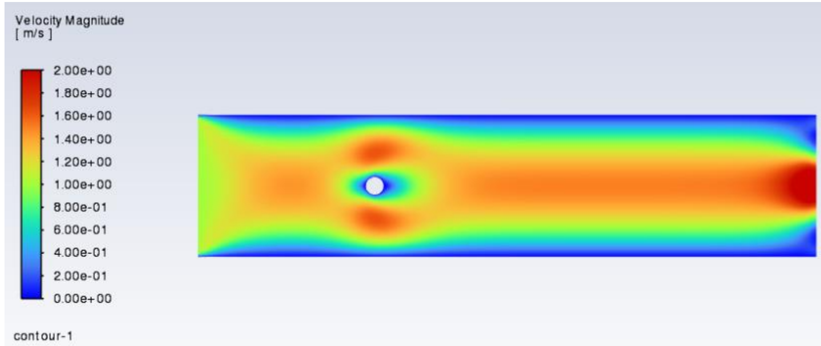

Figure 4a. Velocity magnitude contour at Re = 1 showing slight fore–aft asymmetry as inertial effects begin to influence the flow field.

Figure 4b. Static pressure contour at Re = 1 showing a stronger downstream pressure gradient and increasing pressure-drag contribution.

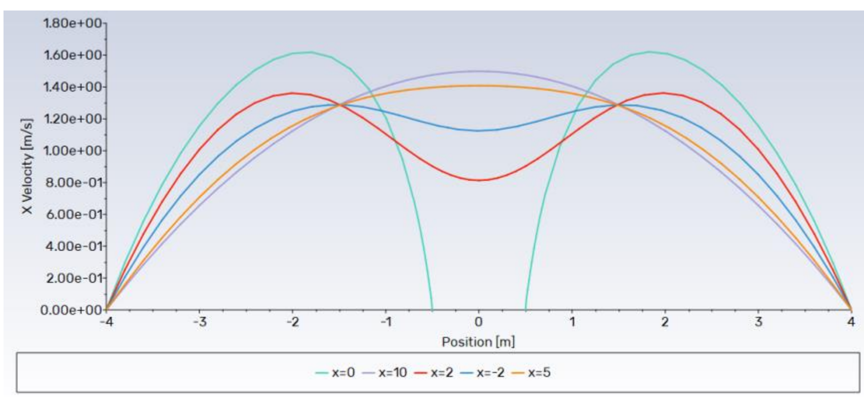

Figure 4c. Streamwise velocity profiles at Re = 1 showing a deeper downstream velocity deficit and early wake development behind the cylinder.

Figure 5. Flow Field at Re = 10 (Steady)

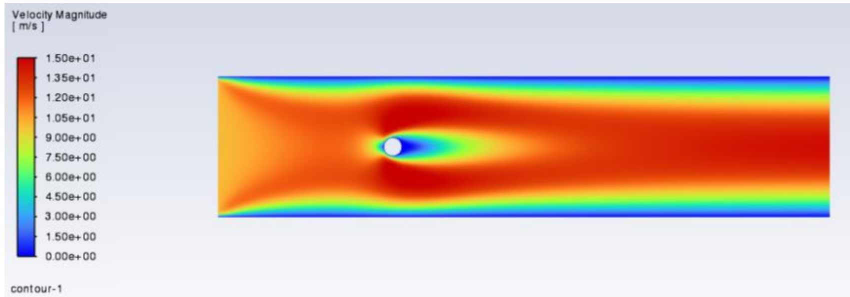

Figure 5a. Velocity magnitude contour at Re = 10 showing a longer downstream wake and increased fore–aft asymmetry as inertial effects become significant.

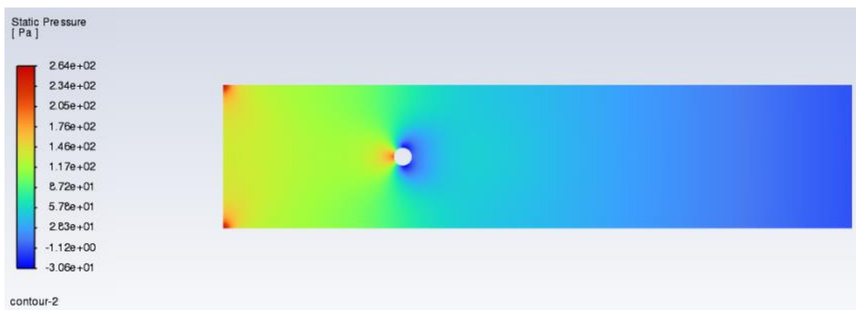

Figure 5b. Static pressure contour at Re = 10 showing a pronounced low-pressure wake region behind the cylinder associated with increasing pressure drag.

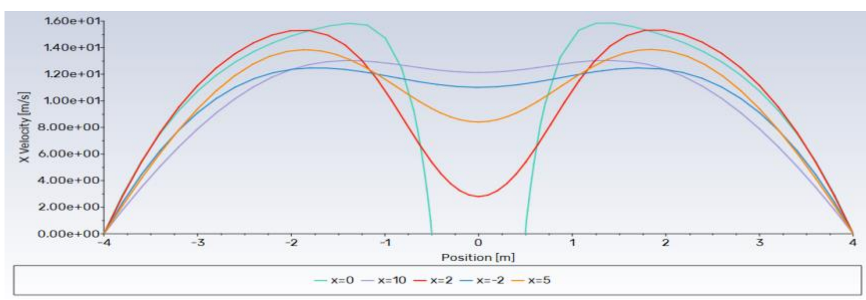

Figure 5c. Streamwise velocity profiles at Re = 10 showing a strong downstream velocity deficit and the onset of a recirculation region behind the cylinder.

Figure 6. Flow Field at Re = 10 (Transient)

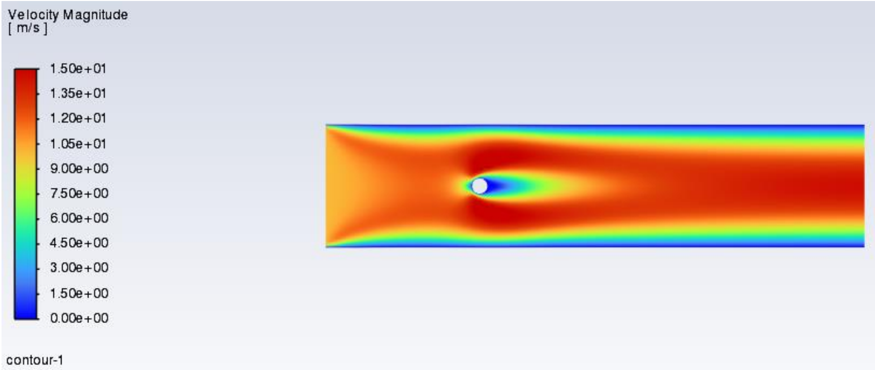

Figure 6a. Velocity magnitude contour at Re = 10 showing a steady attached wake with symmetric recirculation behind the cylinder.

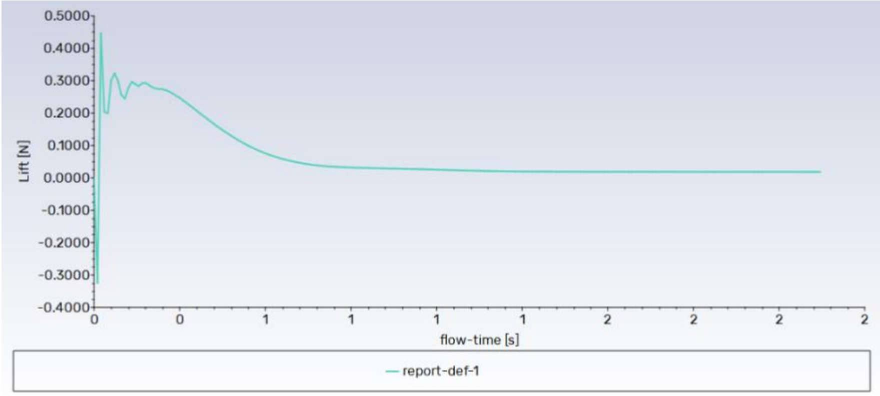

Figure 6b. Lift force history at Re = 10 showing rapid convergence to a constant value with no sustained oscillations, indicating stable flow behavior.

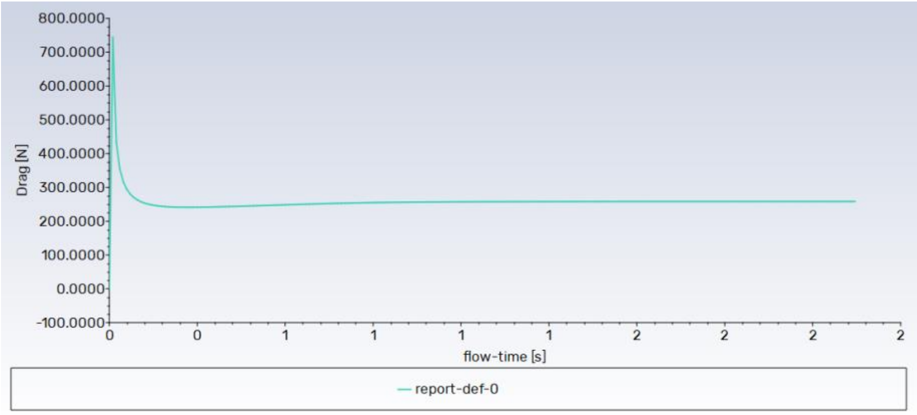

Figure 6c. Drag force history at Re = 10 showing convergence to a steady value without periodic fluctuations, confirming the absence of vortex shedding at this Reynolds number.

Figure 7. Flow Field at Re = 100 (Steady)

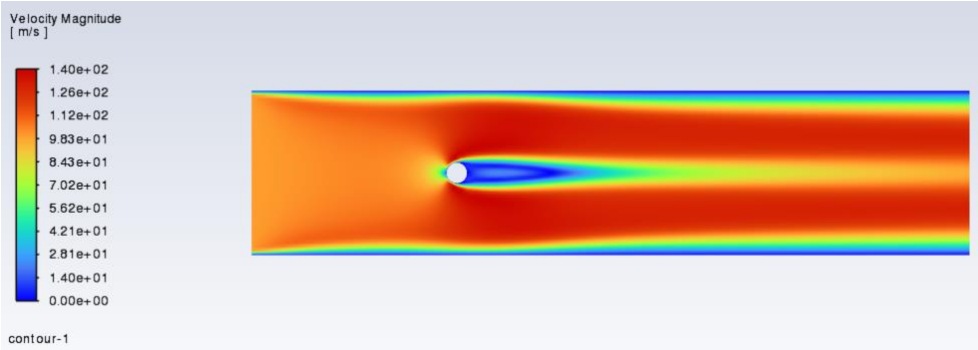

Figure 7a. Velocity magnitude contour at Re = 100 showing a long separated wake and strong downstream velocity deficit behind the cylinder.

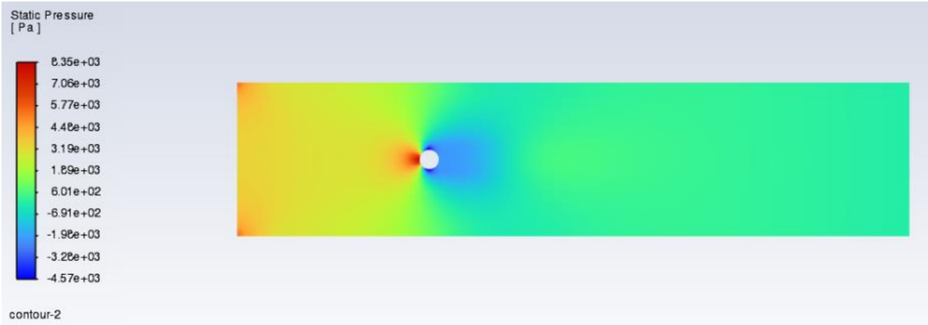

Figure 7b. Static pressure contour at Re = 100 showing a large low-pressure wake region associated with significant pressure drag and flow separation.

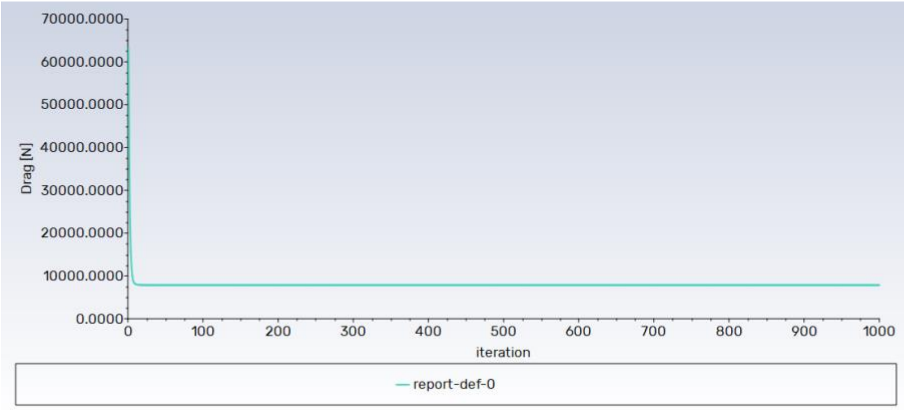

Figure 7c. Drag force convergence history for the steady-state Re = 100 simulation showing convergence to a constant mean value prior to transient analysis.

Figure 8. Flow Field at Re = 100 (Transient)

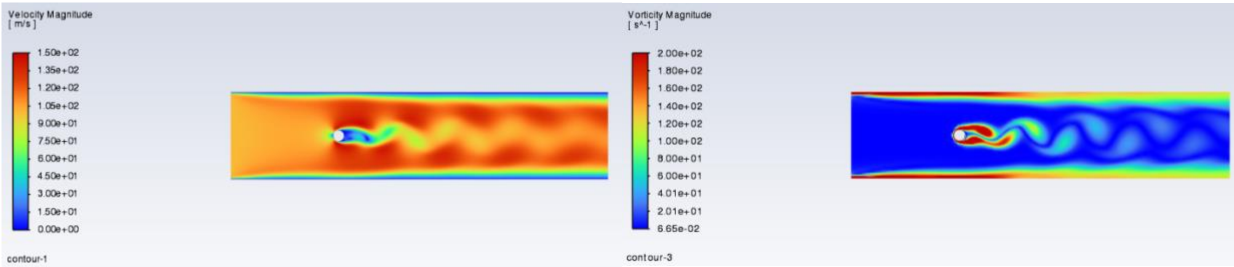

Figure 8a. Velocity magnitude and vorticity contours at Re = 100 showing alternating vortex shedding and the formation of a Kármán vortex street downstream of the cylinder.

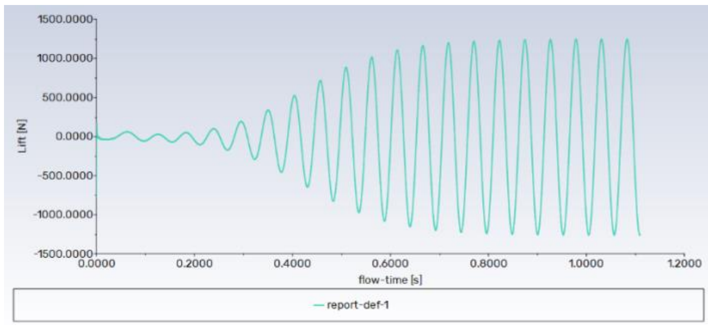

Figure 8b. Lift force history at Re = 100 showing sustained periodic oscillations, confirming the onset of unsteady vortex shedding.

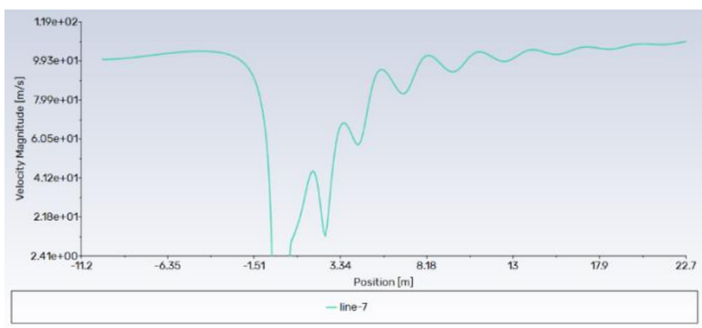

Figure 8c. Centerline velocity magnitude downstream of the cylinder at Re = 100 showing oscillatory wake recovery caused by periodic vortex shedding.

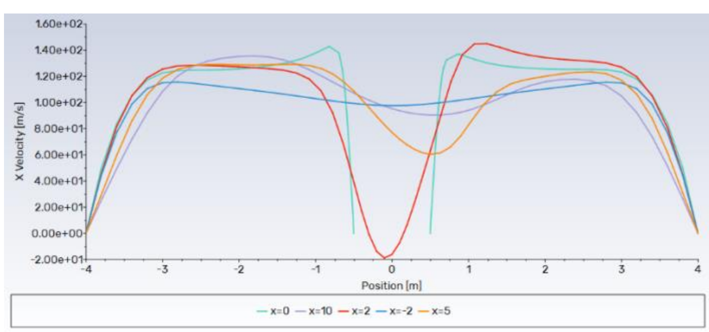

Figure 8d. Streamwise velocity profiles at Re = 100 showing a strong wake velocity deficit, reverse flow behind the cylinder, and delayed downstream recovery caused by periodic vortex shedding.

Figure 9. Flow Field at Re = 1000 (Transient)

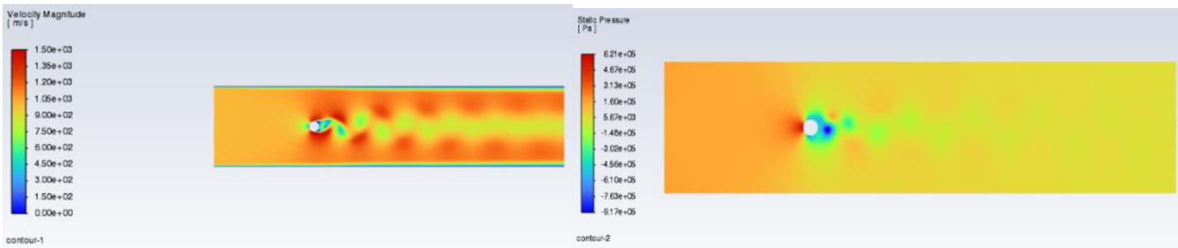

Figure 9a. Velocity magnitude and static pressure contours at Re = 1000 showing a highly unsteady wake with strong alternating vortical structures downstream of the cylinder.

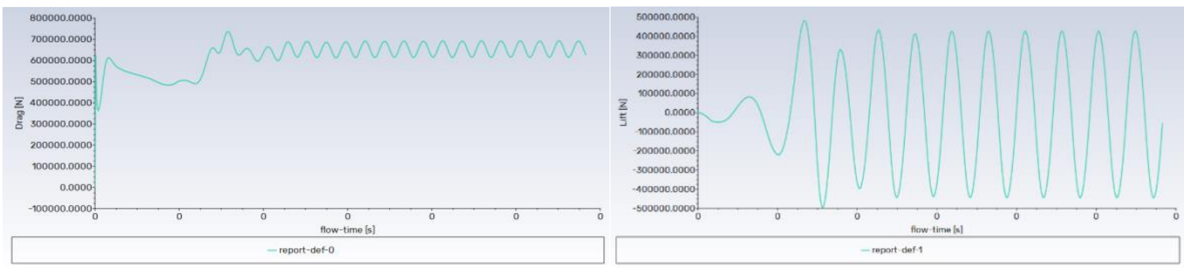

Figure 9b. Drag and lift force histories at Re = 1000 showing large-amplitude periodic oscillations associated with energetic vortex shedding.

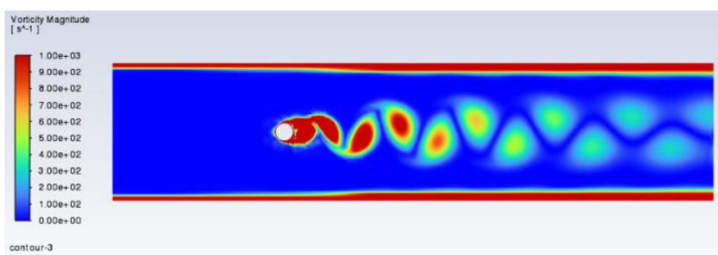

Figure 9c. Vorticity magnitude contour at Re = 1000 showing a fully developed Kármán vortex street extending far downstream of the cylinder.

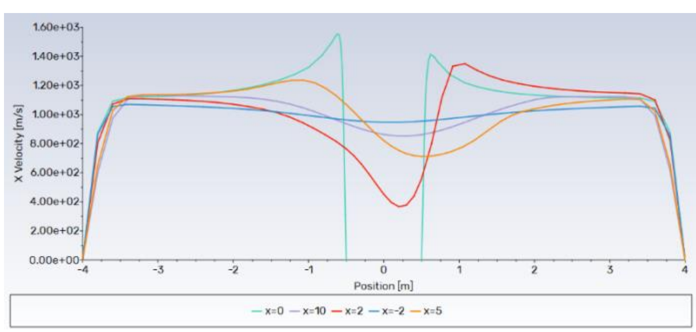

Figure 9d. Streamwise velocity profiles at Re = 1000 showing strong wake velocity deficits and persistent downstream oscillations caused by sustained vortex shedding.

Links to Videos we have produced: MEAM 5360 Re = 100 Transient and MEAM 5360 Re = 1000 Transient